applied sciences

MDPI

Article

Thinned Eisenstein Fractal Antenna Array Using Multi-Objective Optimization for Wideband Performance

Luis E. Cepeda [1], Leopoldo A. Garza [1,*], Marco A. Panduro [2], Alberto Reyna [1] and Manuel A. Zuñiga [1]

[1] Electrical and Electronic Engineering Department, Autonomous University of Tamaulipas, Reynosa 88779, Mexico; a2173720184@alumnos.uat.edu.mx (L.E.C.); alberto.reyna@docentes.uat.edu.mx (A.R.); manuel.zuniga@docentes.uat.edu.mx (M.A.Z.)
[2] Department of Electronic and Telecommunications, CICESE Research Center, Ensenada 22860, Mexico; mpanduro@cicese.mx
* Correspondence: leopoldo.garza@docentes.uat.edu.mx

Abstract: This paper introduces a novel framework for designing wideband antenna arrays using self-similar Eisenstein fractal geometries combined with multi-objective evolutionary optimization techniques. The approach employs multi-objective binary differential evolution (MO-BDE) for array thinning and multi-objective particle swarm optimization (MO-PSO) for optimizing amplitude excitations. This integrated methodology reduces the number of active elements while enhancing overall array performance. The optimization process targets minimizing peak side lobe levels and maximizing directivity over a broad frequency range. Two designs are explored: one optimized at a primary frequency, and another providing consistent wideband behavior. The proposed method achieves a 37.5% reduction in active elements. Design A shows an SLL reduction of −12 dB at the target frequency, while Design B maintains up to −3 dB SLL improvement across the bandwidth. The results confirm the efficacy of the proposed synthesis method for developing scalable, energy-efficient antenna arrays for next-generation systems.

Keywords: antenna array; fractal array; wideband; evolutionary computing; multi-objective optimization

check for updates

Academic Editor: John Xiupu Zhang

Received: 22 April 2025
Revised: 13 May 2025
Accepted: 13 May 2025
Published: 16 May 2025

Citation: Cepeda, L.E.; Garza, L.A.; Panduro, M.A.; Reyna, A.; Zuñiga, M.A. Thinned Eisenstein Fractal Antenna Array Using Multi-Objective Optimization for Wideband Performance. *Appl. Sci.* **2025**, *15*, 5584. https://doi.org/10.3390/app15105584

Copyright: © 2025 by the authors. Licensee MDPI, Basel, Switzerland. This article is an open access article distributed under the terms and conditions of the Creative Commons Attribution (CC BY) license (https://creativecommons.org/licenses/by/4.0/).

1. Introduction

Fifth-generation (5G) communication has brought substantial enhancements to telecommunication systems, offering higher transmission rates and more efficient spectrum utilization. However, with the continuous evolution of technologies and the impending arrival of sixth-generation (6G) networks, there is a growing need for more advanced and efficient solutions [1]. In this context, the design and optimization of antenna array systems play a critical role in maximizing physical resource utilization and enabling greater control over signal directionality, noise mitigation, and other interferences. These advancements support practical applications such as ultra-reliable low-latency communication (URLLC), large-scale Internet of Things (IoT) deployments, sensor networks, and radar systems [2,3]. Emerging technologies such as multiple-input multiple-output (MIMO), reconfigurable intelligent surfaces (RISs), and edge computing have facilitated the development of more complex antenna arrays with an increased number of elements. Simultaneously, improvements in computational power and optimization algorithms have expanded the possibilities for antenna design, enabling the exploration of novel geometries. Among these, fractal geometries have gained significant attention for their ability to support broader bandwidths and higher element densities [4].

The application of fractal geometry in antenna array design has seen rapid growth, driven by the intrinsic advantages that these structures offer. Notably, fractal-based arrays exhibit enhanced multiband operation, scalability for large-element configurations, and potential for miniaturization [5]. These characteristics are particularly advantageous for technologies such as MIMO and wideband, which have shown notable performance improvements in data transmission and spectral efficiency. The advancement of computational methods and design tools has further accelerated research in this area, enabling the investigation of innovative fractal structures and optimization strategies, and facilitating the design of increasingly complex and efficient arrays [6].

The incorporation of fractal geometry into antenna design began in the 1990s due to the favorable relationship between self-similar structures and frequency-independent behavior, which directly supports wider bandwidths [7]. These properties are preserved when fractal geometry is applied to the spatial distribution of array elements, leading to the development of fractal antenna arrays. Such arrays have demonstrated strong performance and are considered a viable alternative to conventional designs, offering improvements in both bandwidth and spatial efficiency [5,8].

Early studies such as [9–12] evaluated the effectiveness of well-known fractals previously applied to individual antenna elements, including the Gosper curve, Fudgeflake, Cantor set, and Sierpinski fractals in the design of antenna arrays. Subsequent research introduced optimization algorithms to further improve array performance. For instance, ref. [13] proposed a broadband array design based on the space-filling Peano–Gosper curve, optimizing the element distribution to enhance bandwidth across different curve iterations. Similarly, ref. [14] employed self-similar geometries with rotational symmetry to suppress grating lobes in ultra-wideband (UWB) arrays, using a covariance matrix adaptation evolutionary strategy (CMA-ES).

More recent studies, such as [15,16], introduced innovative methodologies for designing fractal antenna arrays. These approaches achieved high performance without increasing structural complexity, utilizing self-similar geometry-based fractal generators in heptagonal, hexagonal, and pentagonal configurations. Circular and spiral self-similar concentric ring arrays were explored in [17,18], where differential evolution (DE) and particle swarm optimization (PSO) algorithms were applied to optimize element distribution. These techniques enabled the development of compact array structures with improved bandwidth and greater control over element placement. In [19], a fractal-based MIMO radar array was implemented using a combination of Fudgeflake and Gosper Island geometries to form transmit and receive sub-arrays. This configuration created virtual elements that enhanced angular resolution and suppressed sidelobes.

Previous works in antenna array synthesis have shown that effective sidelobe-level (SLL) suppression plays a critical role in reducing interference, improving signal-to-noise ratio (SNR), and enhancing realized gain in targeted directions. Techniques such as weighted multi-beam synthesis [20] and multi-beam transmit array design for 5G platforms [21] have demonstrated that improving pattern control not only suppresses SLL but also contributes to better spectral efficiency and spatial reuse.

The application of Eisenstein geometry and Eisenstein-based fractals in wideband array design was first introduced in [22]. This approach builds upon the Eisenstein integer packing described in [23], which uses a set of complex numbers to form a hexagonal lattice that uniformly fills the complex plane, ensuring equal spacing between adjacent elements, facilitating array miniaturization and reducing mutual interference. The research in [22] involved analyzing multiple fractal stages with arrays of 16, 64, 256, and 1024 elements. In that prior study, array thinning was performed using a genetic algorithm combined with least mean squares (GA-LMS) optimization, resulting in sub-aperture designs at each fractal

stage. The thinned arrays with 10, 40, 160, and 640 elements prioritized sidelobe-level (SLL) minimization at a single operating frequency, at the cost of reduced performance across wideband frequencies.

This work aims to advance antenna array design for wideband applications by leveraging the geometric characteristics of Eisenstein fractals. The methodology focuses on optimizing wideband performance while minimizing the number of active elements through efficient spatial packing and array thinning. By capitalizing on the self-similarity and hexagonal symmetry inherent to Eisenstein geometry, a scalable and performance-optimized approach to array configuration is introduced.

The remainder of this paper is structured as follows. Section 2 presents the proposed methodology for antenna array design, including a detailed description of the Eisenstein fractal generator (Section 2.1), the array factor formulation and parameter calculations (Section 2.2), and the proposed multi-objective wideband optimization framework (Section 2.3). Section 3 reports the simulation results for two design scenarios, evaluating their performance across different fractal growth stages. Section 4 discusses the comparative advantages of the proposed designs relative to existing wideband antenna array methodologies. Finally, Section 5 concludes the paper by summarizing the main findings and outlining potential directions for future research.

2. Methodology

The proposed methodology presents a structured framework for designing thinned wideband antenna arrays based on Eisenstein fractal geometry that utilizes the self-similarity properties of the geometry in combination with an optimization process guided by evolutionary optimization techniques. The primary objective is to minimize the number of active elements while preserving high performance characterized, by low sidelobe levels and stable directivity across a wide frequency range.

2.1. The Eisenstein Fractal Generator

The Eisenstein fractal was previously introduced in [23], where it is represented as a subset of Eisenstein integers; this set is denominated as the Eisenstein domain, which is characterized by its hexagonal lattice grid. Eisenstein integers are complex numbers of the form $z = a + b\omega$, where a, b are real integers and ω is a primitive cube root of unity given by $\omega = e^{2\pi i/3}$.

The Eisenstein fractal at a given growth stage p is represented by the set of points S_p. The initial stage ($p = 1$) is defined by the vertex set $v = \omega^2, \omega^1, \omega^0, 0$, as illustrated in Figure 1, which establishes the base geometry of the fractal generator. For higher stages ($p > 1$), the generator is constructed by replicating the previous stage's point set at each vertex, incorporating a rotation pattern $r_p = e^{(p-1)\pi i/3}$ (60°) and a scaling factor $\delta_p = 2^{p-1}$ corresponding to the growth level. The points for the subsequent stage are recursively defined in terms of the previous stage as follows:

$$S_{p+1} = \bigcup_{v} S_p + (\delta_p \cdot r_p \cdot v) \tag{1}$$

The equation for the generator at any growth stage is described as

$$S_P = \bigcup_{v} \left(\sum_{p=1}^{P} 2^{(p-1)} \cdot e^{(p-1)\pi i/3} \cdot v \right) \tag{2}$$

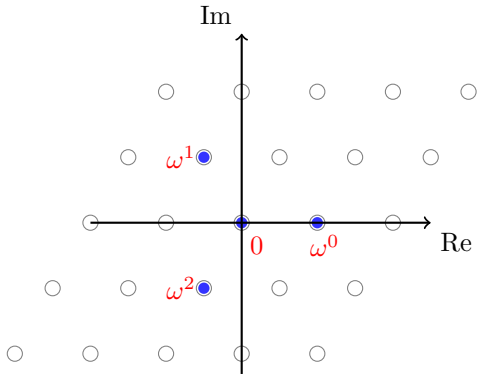


Figure 1. Eisenstein domain lattice showing first Eisenstein integers 0, ω^0, ω^1, ω^2.

The Eisenstein fractal evolves through recursive geometric transformations and is described by the point set S_p. In Equation (1), the operator $\bigcup_v$ denotes a union over all base vertices $v \in \{\omega^2, \omega^1, \omega^0, 0\}$. The term $S_p + (\delta_p \cdot r_p \cdot v)$ represents a translation of the entire point set S_p, where the translation vector is computed by scaling and rotating the vertex v. Specifically, the scaling factor δ_p controls the growth size at stage p, and the rotation factor r_p applies a complex exponential rotation by 60° increments, preserving the hexagonal symmetry of the Eisenstein lattice. Equation (2) expresses this recursive process in a closed form. Here, the inner summation sequentially applies the same scale and rotation operations used in the recursive definition, accumulating the transformation effects across all stages from 1 to P. The outer union $\bigcup_v$ again distributes these transformations across each vertex v, generating the complete point set S_P.

The recursive geometric construction of the Eisenstein fractal across successive growth stages is represented in Figure 2, where each new stage replicates the previous stage's structure around rotated and scaled versions of the Eisenstein integer vertices. Table 1 lists the complex coordinates $a + jb$ of the Eisenstein integers used at stage $p = 2$. Each entry in the table corresponds to a specific vertex location generated by linear combinations of scaled roots ω^k, revealing the structured placement of elements in the generator.

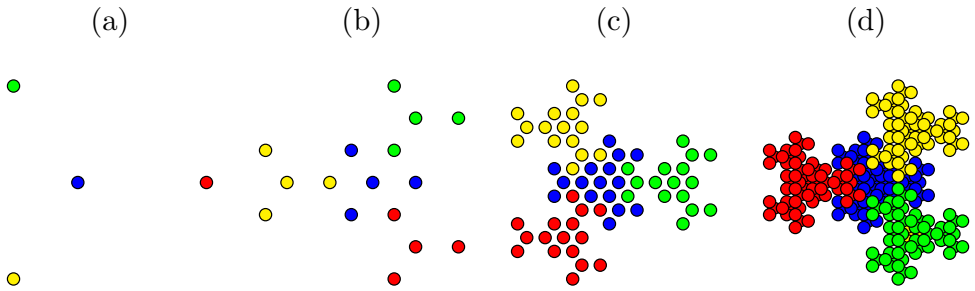


Figure 2. Geometric construction of the Eisenstein fractal array across growth stages, showing recursive replication at rotated vertices for stages: (**a**) $p = 1$, (**b**) $p = 2$, (**c**) $p = 3$, (**d**) $p = 4$.

The self-similar nature of fractal geometry allows each iteration of a structure to be systematically derived from its preceding stage, streamlining element distribution as the array scales to larger configurations. In antenna array design, this property facilitates the development of large-scale arrays that retain geometric uniformity and modularity. In this study, we leverage the inherent self-similarity of Eisenstein fractals in conjunction with array thinning techniques to maintain wideband performance while significantly reducing the number of active elements.

To construct thinned antenna arrays across multiple fractal growth stages, we introduce two structural transformation mechanisms based on the underlying fractal generator.

Both strategies utilize an optimized base configuration from a lower-order stage as the foundation for generating more complex thinned structures.

Table 1. Complex coordinates of Eisenstein integers at fractal growth stage 2. Indices correspond to element placement in the array generator.

Index	ω	$a + jb$
1	0	$0.00 + 0.00$i
2	1	$1.00 + 0.00$i
3	ω^1	$-0.50 + 0.866$i
4	ω^2	$-0.50 - 0.866$i
5	$2\omega^{1/2}$	$1.00 + 1.732$i
6	$2\omega^{1/2} + 1$	$2.00 + 1.732$i
7	$2\omega^{1/2} + \omega^1$	$0.50 + 2.598$i
8	$2\omega^{1/2} + \omega^2$	$0.50 + 0.866$i
9	$2\omega^{3/2}$	$-2.00 + 0.00$i
10	$2\omega^{3/2} + 1$	$-1.00 + 0.00$i
11	$2\omega^{3/2} + \omega^1$	$-2.50 + 0.866$i
12	$2\omega^{3/2} + \omega^2$	$-2.50 - 0.866$i
13	$2\omega^{5/2}$	$1.00 - 1.732$i
14	$2\omega^{5/2} + 1$	$2.00 - 1.732$i
15	$2\omega^{5/2} + \omega^1$	$0.50 - 0.866$i
16	$2\omega^{5/2} + \omega^2$	$0.50 - 2.598$i

The first method, referred to as the self-replication property, duplicates the thinned base structure at each vertex defined by the generator equation, enabling higher-order stages to be assembled through modular subarray repetition. The second method, termed the upscaling property, applies a geometric scaling transformation to the base structure. A replica of the previous-stage point set is then positioned at each upscaled location, embedding the prior optimized layout within a larger configuration. This method enables the controlled expansion of element distribution while preserving key performance characteristics across successive growth stages (Figure 3).

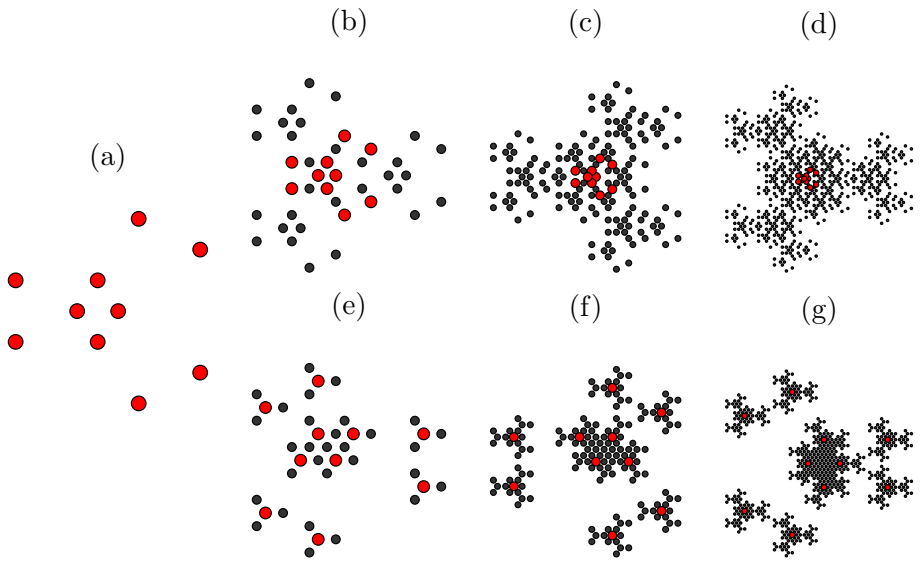


Figure 3. Illustration of thinned Eisenstein fractal array layouts using two structural transformation methods: (**a**) base structure, (**b**–**d**) recursive self-replication across stages $p = 3$ to $p = 5$, and (**e**–**g**) geometric upscaling across the same stages.

Both of these properties are explored as strategies for reducing the number of active antenna elements while preserving the wideband characteristics of the Eisenstein fractal antenna array. These transformation methods streamline the design for large-scale arrays by enabling more efficient and organized element configurations. The self-replication property facilitates a modular design approach, where subarrays are systematically replicated across the fractal geometry. This results in higher-order configurations that maintain structural coherence and support scalable performance.

2.2. Array Factor and Parameter Calculation

The far-field radiation performance of an antenna array is primarily determined by its array factor (AF), which depends on the geometric configuration of the antenna structure, the relative amplitudes, and the phase shifts applied to each individual element [24,25]. For a two-dimensional antenna array composed of N antenna elements positioned in the complex plane, each element's location Z_N can be represented by a complex number $x_n + jy_n$. Thus, the array factor $AF(\theta)$ for this configuration is mathematically expressed as follows:

$$AF(\theta, \phi_0) = \sum_{n=1}^{N} I_n e^{ik(x_n \cos(\theta)\cos(\phi_0) + y_n \cos(\theta)\sin(\phi_0))} \quad (3)$$

where $k = \frac{2\pi}{\lambda}$ describes the wavenumber and the wavelength λ of the frequency of evaluation for the array factor. The amplitude excitation I_n of the nth element and its position are represented in Cartesian coordinates. The cos and sin operators describe the phase shifts along their respective axes, considering no steering angle in elevation (θ_0) and azimuth cut angle $\phi_0 = 90°$.

Throughout the optimization process, $AF(\theta)$ is evaluated from 0 to π , assuming symmetrical responses in the lower hemisphere [25]. The operational bandwidth is defined by the ratio of the upper frequency limit to the lower frequency limit within which the AF maintains an acceptable SLL performance.

2.3. Optimization Process

The employed optimization process consists of a two-step implementation of an evolutionary algorithm framework, where Binary Differential Evolution (BDE) is employed to determine the activation states of individual antenna elements; then, Particle Swarm Optimization (PSO) is used to fine-tune the configuration of amplitude excitations. The hybrid approach leverages their strengths: MO-BDE excels in the exploration of different configurations, while MO-PSO offers fast convergence, ideal for fine-tuning amplitude weights in large-scale arrays. These algorithms are chosen for their proven effectiveness in addressing nonlinear, multi-objective optimization problems, particularly in array synthesis tasks [26–29]. When combined with the dense packing and self-similar properties of Eisenstein fractal geometry, this approach enables precise control over critical performance parameters such as SLL and half-power beamwidth (HPBW), resulting in efficient and scalable antenna array configurations.

The optimization process for achieving wideband performance is carried out using the lower and upper frequency boundaries (f_l, f_u) as targets to ensure consistent radiation characteristics across the entire operational bandwidth. The operational lower frequency f_l is defined by the normalized spatial ratio $d/\lambda = 0.5$ and the upper frequency f_u is defined by $d/\lambda = 2$, where d is the spacing between elements of the array, $f = c/\lambda$ is the frequency relation, and c is the constant of light propagation velocity [22]. As demonstrated in [13], optimizing the array at the upper frequency limit has a positive impact on performance at lower frequencies. Building upon this insight, the present work adopts a multi-objective optimization strategy aimed at enhancing the array response at the initial operating frequency

while simultaneously preserving wideband behavior and minimizing the peak sidelobe level (SLL) [30]. The proposed optimization framework utilizes multi-objective functions to balance key design trade-offs, including element thinning, SLL suppression, and directivity enhancement in both frequency boundaries. Through the application of a mask function, it enforces constraints on the radiation pattern, encouraging a more uniform energy distribution across the angular spectrum. Lowering the peak SLL is critical for reducing interference and improving the overall quality of the radiation pattern [20,29,31,32].

The objectives for thinning optimization in Algorithm 1 and excitation amplitude optimization in Algorithm 2 are

$$OBJ_1 = \frac{1}{n}\sum_{i=1}^{n}\Big(AF_{f_l}(\theta_i) - MASK_{f_l}(\theta_i)\Big)^2 \tag{4}$$

$$OBJ_2 = \frac{1}{n}\sum_{i=1}^{n}\Big(AF_{f_u}(\theta_i) - MASK_{f_u}(\theta_i)\Big)^2 \tag{5}$$

$$OBJ_3 = 1 + [N_T - N]^2 \tag{6}$$

Equations (4) and (5) define the objective functions used to minimize beamforming error at two operating frequencies, f_l and f_u, respectively. Each equation computes the mean squared deviation between the actual array factor AF_f and a reference mask $MASK_f$ over n angular samples θ_i. $MASK_f$ is derived from the main beam shape of the original AF_f response (no turned-off elements and no amplitude weights), where all sidelobe regions are replaced by a constant value corresponding to the target SLL. A target reduction of -10 dB was applied across different stages and frequencies to define the desired envelope. The term $(AF_f(\theta_i) - MASK_f(\theta_i))^2$ quantifies the squared error at each angular direction, and the summation accumulates this error across all directions, forming a least-mean-square-error (LMSE) criterion that ensures the radiation pattern conforms to the desired shape, suppressing SLL while maintaining main-lobe integrity.

Algorithm 1 MO-BDE for Antenna Array Thinning

Initialization: Generate an initial binary population representing active/inactive elements.
Evaluation: Compute objective functions: **OBJ1**, **OBJ2**, and **OBJ3**.
Ranking: Sort non dominated fronts and identify elite leaders from first front.
for each non-elite individual **do**
  Select three random elite solutions.
  Generate a donor vector via bitwise logic (XOR/AND) from selected individuals.
  Perform crossover and mutation to generate a trial solution.
  Re-evaluate trial on all objectives.
  if trial solution dominates current **then**
    Replace original with trial.
  end if
end for
Return: Updated binary population representing optimized thinning configurations.

Equation (6) defines the OBJ_3 function, a penalty term designed to regulate the number of active elements in the antenna array. In this formulation, N_T denotes the number of active elements in the current configuration, while N represents the desired number of elements for array thinning. The term $(N_T - N)^2$ imposes a penalty on deviations from the target sparsity level, thereby guiding the optimization process toward solutions with a controlled number of active elements. The inclusion of a constant term (1) ensures that the function remains strictly positive, maintaining its significance within the multi-objective optimization framework. The use of OBJ_3 enables solutions with various thinning ratios

to be evaluated through non-dominated sorting, facilitating the exploration of diverse trade-offs between array sparsity and radiation performance.

MO-BDE is employed for its effectiveness in binary-state optimization and its strong exploratory capability within the solution space. In contrast, MO-PSO is well-suited for continuous parameter tuning such as amplitude weights, with demonstrated efficiency and convergence in large-scale configurations. This hybrid strategy exploits the strengths of both algorithms while maintaining low computational overhead.

Algorithm 2 MO-PSO for Amplitude Excitation Tuning

1: **Initialization:** Create swarm of particles with integer amplitude weights [1–10] for active elements.
2: **Evaluation:** Compute objective functions: **OBJ1** and **OBJ2**.
3: **Ranking:** Sort non dominated fronts and identify elite leaders.
4: Assign initial personal best ($pBest$) for each particle and select global best ($gBest$) from elite set.
5: **for** each non-elite particle **do**
6: Update velocity using inertia weight w, cognitive component $c_1 \cdot (pBest - position)$, and social component $c_2 \cdot (gBest - position)$.
7: Apply stochastic mutation to velocity for exploration.
8: Update particle position and re-evaluate fitness.
9: Update $pBest$ if improved.
10: **end for**
11: **Adaptation:** Adjust parameters (w, c_1, c_2) based on convergence rate.
12: **Return:** Population with optimized excitation weights for active elements.

Figure 4 outlines the complete framework implementation. The multi-objective strategy is demonstrated in two design cases, reinforcing the structural transformation properties. This approach enables optimized array configurations that balance performance trade-offs across frequency bands, ensuring both spectral efficiency and stable radiation patterns.

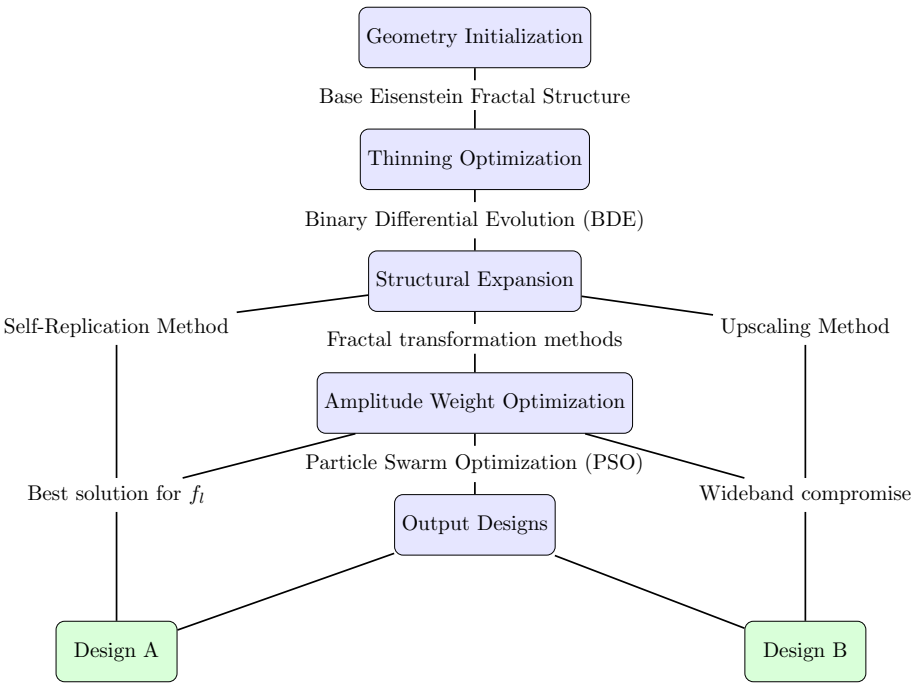


Figure 4. Framework optimization flowchart for proposed designs.

While the Eisenstein fractal geometry inherently supports dense packing with uniform inter-element distances, a lower bound on spacing is typically imposed to neglect mutual

coupling effects, which can distort the radiation pattern performance. In the present implementation, amplitude excitation weights are rounded to integer values between 1 and 10 to minimize quantization errors and simplify calibration. Moreover, the optimization framework employs amplitude tapering alone, excluding phase shift control to avoid the complexity of the feeding network on such large scale arrays.

3. Results

Simulations, performance assessments, and the implementation of the optimization algorithms were carried out within the MATLAB R2023a environment on a workstation system with an AMD Ryzen 5 5600X processor, 32 GB DDR5 RAM, and an NVIDIA RTX 2060 GPU. The parameter calibration process for the MO-BDE and MO-PSO algorithms is detailed in Table 2; specific configurations were refined to enhance optimization efficacy.

Table 2. Simulation and algorithm parameters.

SIMULATION PARAMETERS	
Population size	2000
Number of generations	2000
Evaluation angle samples (θ)	1440
Fractal structure stages	$p = 2$ $p = 3$ $p = 4$ $p = 5$
Individual gene size	$N = 16$ $N = 64$ $N = 256$ $N = 1024$
MO-BDE	
Thinning factor	0.625
Differential weight parameter (F)	2
Crossover probability (C_R)	0.75
Mutation probability (M_R)	$\frac{1}{2 \cdot N}$
Average duration at stages	30 m 85 m 160 m 760 m
MO-PSO	
Amplitude weight values	$x \in \mathbb{Z} \mid 1 \leq x \leq 10$
Initial inertia weight	$\omega_0 = 2$
Initial acceleration coefficient	$c_1 = 1.6$ $c_2 = 1.4$
Average duration at stages	6 m 35 m 82 m 260 m

The multi-objective implementation incorporating the three defined objective functions is visualized in Figure 5. In Figure 5a, candidate solutions satisfying $N = N_T$ are in blue, while non-candidate solutions are colored along a gradient to red, indicating the deviation from the desired target. The evaluation of the initial solution is depicted in black. In this graph, the first Pareto front of the three-dimensional solution space is projected onto a 2D plane, where the thinning objective is represented through a color mapping. The figure illustrates how non-candidate solutions with $N \neq N_T$ can still contribute to the exploration process, enhancing the overall search by promoting diversity in the solution space. Figure 5b presents the solutions for the excitation tuning phase using the MO-PSO algorithm. This plot shows the obtained first Pareto front in the OBJ_1–OBJ_2 space, where the dense clustering of optimized solutions toward the lower-left corner reflects successful convergence, where both objectives are minimized.

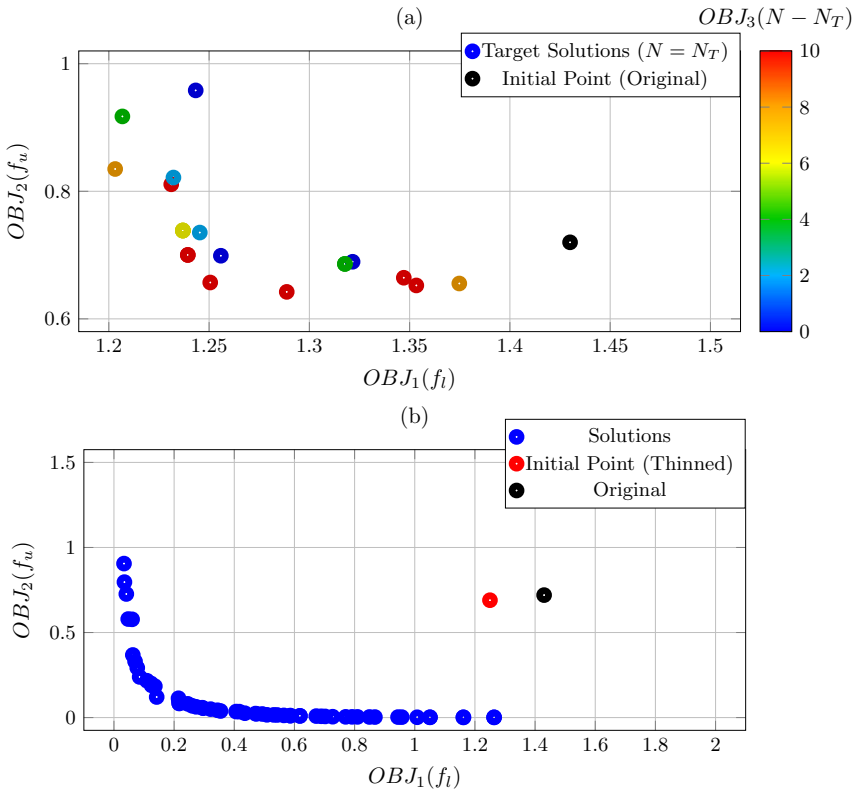


Figure 5. Solution space and convergence of algorithms; (**a**) MO-BDE for array thinning and (**b**) MO-PSO for amplitude weight tuning

The implementation of the mask function is illustrated in Figure 6. The plots are presented at frequency boundaries, (f_l) and (f_u). Corresponding mask functions are applied to minimize SLL while maintaining the integrity of the main lobe. The resulting array factor (AF) is designed to mitigate secondary-lobe interference and promote a more uniform distribution of radiated energy across the intended coverage region.

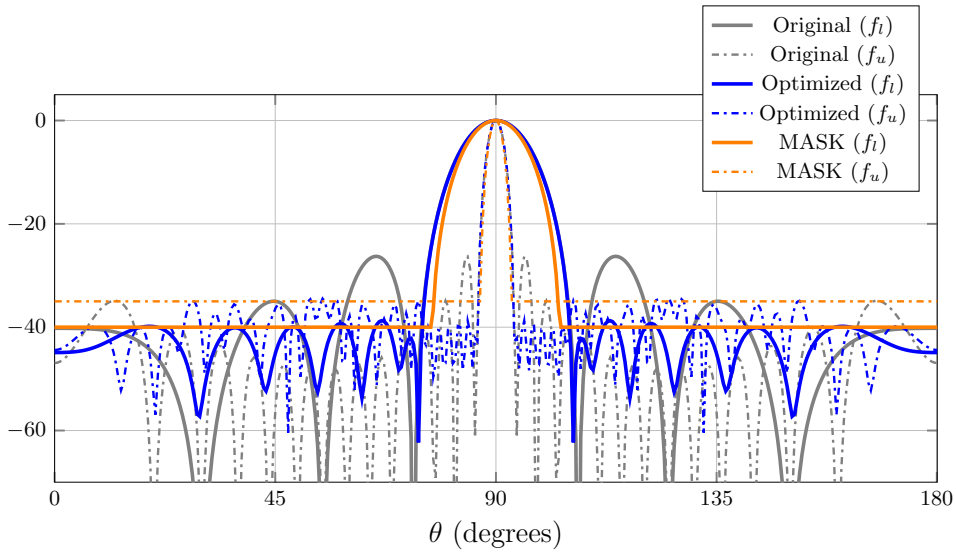


Figure 6. Array factor performance of optimized pattern and original array using mask function objectives at stage 4.

The proposed optimization framework is applied to two design scenarios to evaluate the capabilities of the Eisenstein fractal geometry and the wideband optimization approach.

By leveraging the first front of the multi-objective solution set, optimal configurations can be selected to meet distinct design objectives. Optimization at f_u results in balanced performance across the entire bandwidth, while targeting f_l leads to enhanced performance at the initial operating frequency, though with potential trade-offs in effectiveness at higher frequencies:

1. Design A: initial frequency optimization (f_l);
2. Design B: wideband compromise optimization (f_l to f_u).

Design A prioritizes optimization at the initial operating frequency f_l, making it well-suited for applications that demand high precision and stability within a defined baseband. This design approach may partially compromise wideband performance in favor of enhanced behavior at the operational frequency. Conversely, Design B aims to achieve a balanced radiation response across the operational bandwidth, making it more appropriate for applications requiring frequency agility and consistent performance over a wider range.

For higher fractal stages ($p \geq 3$), thinned array configurations are generated by applying the self-replication and upscaling properties to the optimized stage 2 structure. This hierarchical approach has shown improved results compared to direct optimization at higher stages. Findings indicate that the self-replication method enhances performance at the operational design frequency, while the upscaling method maintains a more uniform response across the array bandwidth.

Table 3 provides a comparative analysis of performance metrics for the proposed Designs A and B, the complete Eisenstein fractal array configurations with 64 and 256 elements, and conventional uniform square planar arrays with equivalent element counts. The comparison highlights the advantages of employing the Eisenstein fractal geometry for wideband applications.

Table 3. Performance comparison of the proposed optimized designs (Design A and B) against the original Eisenstein fractal array and a conventional uniform planar array.

Array Structure	Elements	Bandwidth	SLL at f_l (dB)	SLL over Bandwidth (dB)
Planar	64	1:1	−12.76	–
	256	1:1	−13.14	–
Original Eisenstein	64	4:1	−25.59	−25.59
	256	4.2:1	−26.29	−26.28
Design A	40	4:1	−38.72	−19.25
	160	4.2:1	−38.74	−34.55
Design B	40	4:1	−27.17	−27.17
	160	4.2:1	−29.86	−29.83

The proposed designs demonstrate improved performance in terms of SLL reduction and directivity, despite using fewer active elements. These results validate the effectiveness of the proposed optimization methodology and underscore its potential for developing efficient, wideband antenna arrays. The analysis focuses on stages 3 and 4 of the proposed designs, where the number of active elements remains within a practical range that is feasible for fabrication and appropriate for experimental prototyping.

Figure 7 presents the wideband SLL performance comparison between Design A, Design B, and the original 64-element Eisenstein configuration. The results demonstrate notable improvements in SLL suppression, even with a reduced number of active elements. Design A achieves a significant reduction of approximately −10 dB in SLL at the initial operating frequency f_l, with a trade-off of about 2 dB degradation across the broader

bandwidth. In contrast, Design B maintains a more consistent performance, achieving an SLL reduction of approximately −3 dB across the entire operational frequency range.

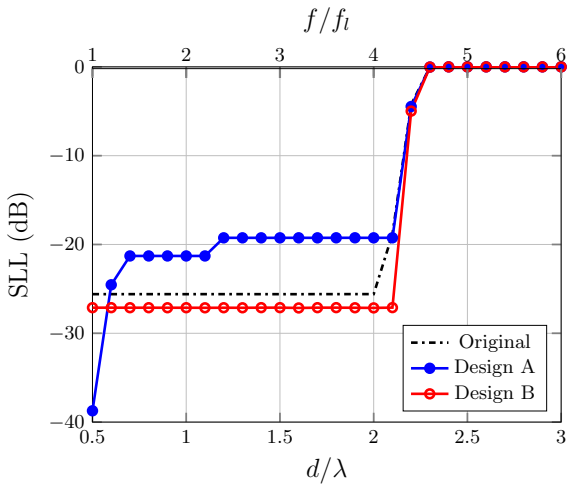


Figure 7. Peak sidelobe-level (SLL) comparison across normalized frequency range for Design A and Design B with 40 elements and original Eisenstein fractal structure with 64 elements at stage 3.

The array factor (AF) performance of both proposed designs at the frequency boundaries f_l and f_u is illustrated in Figure 8. Design A exhibits excellent performance at f_l, with significantly reduced SLL, while still maintaining acceptable behavior at f_u, despite the reduced element count. Design B delivers improved performance at both frequency boundaries, achieving a narrower main beamwidth and enhanced directivity, all while maintaining a lower number of active elements. These results highlight the effectiveness of the proposed optimization strategy in balancing bandwidth, directivity, and element count. Figure 9 shows the wideband SLL performance for each stage of both designs.

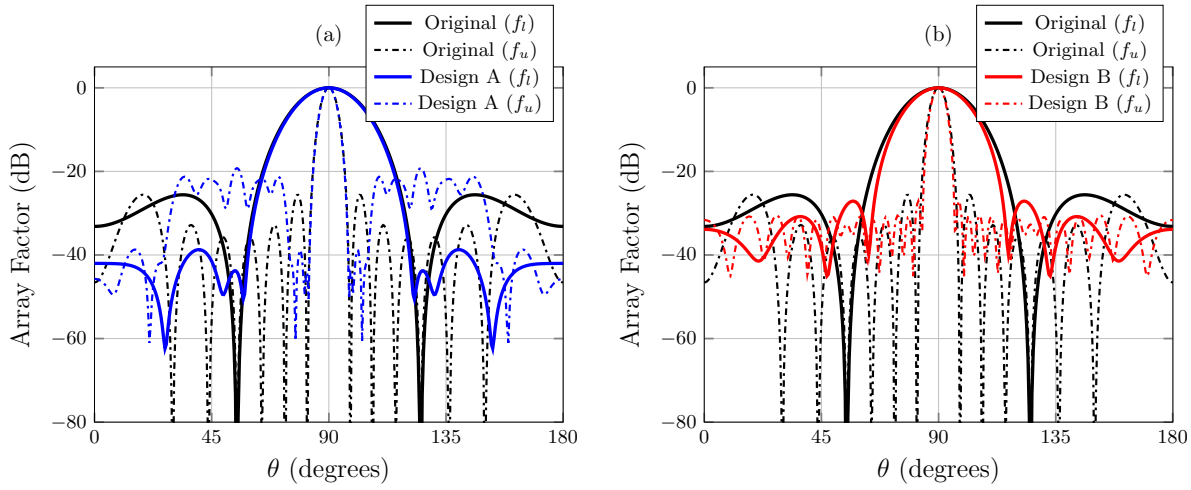


Figure 8. Array factor (AF) patterns at frequency boundaries f_l and f_u for stage 3 arrays: (**a**) Design A vs. original array, (**b**) Design B vs. original array.

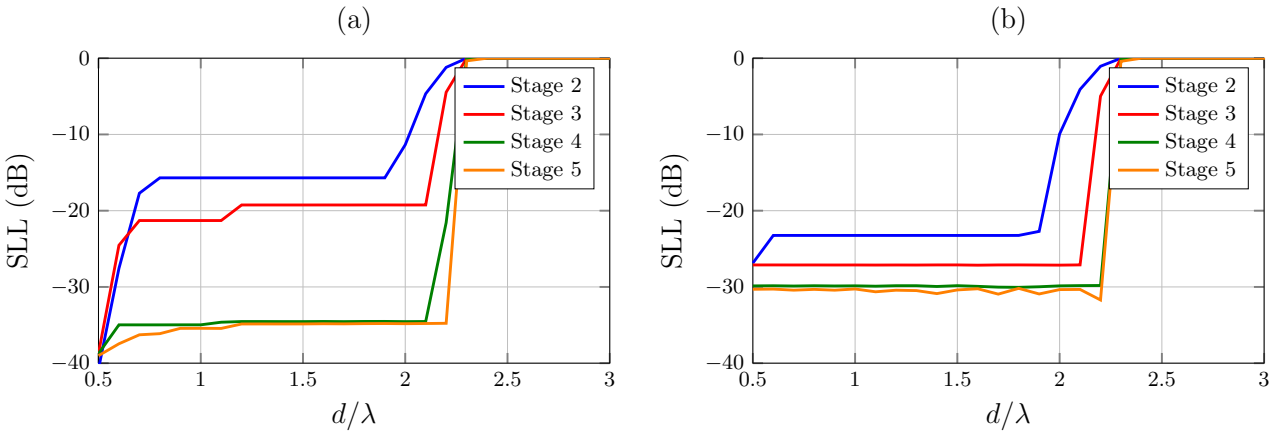


Figure 9. Wideband SLL performance for (**a**) Design A and (**b**) Design B across fractal growth stages $p = 2$ to $p = 5$.

The element layouts for the proposed thinned arrays are illustrated using color mappings that represent the amplitude excitation applied to each element (Figure 10). These visualizations correspond to the optimal configurations of active (on) and inactive (off) elements, along with their respective excitation amplitudes, optimized to enhance the radiation pattern at the initial operating frequency. For growth stages 3, 4, and 5 of Design A, a self-replicated subarray approach is employed to construct the array, effectively reducing structural complexity. Following this structural replication, amplitude optimization is performed on the resulting array to satisfy the dual-objective criteria.

Similarly, the array configurations for Design B in stages 3, 4, and 5 are generated by upscaling the optimized base structure. Amplitude values are then re-optimized for each stage to maintain SLL suppression across the entire bandwidth (Figure 11). These design strategies enable scalable and systematic array construction for higher fractal stages, preserving the same thinning ratio while maintaining consistent frequency response characteristics in both design cases.

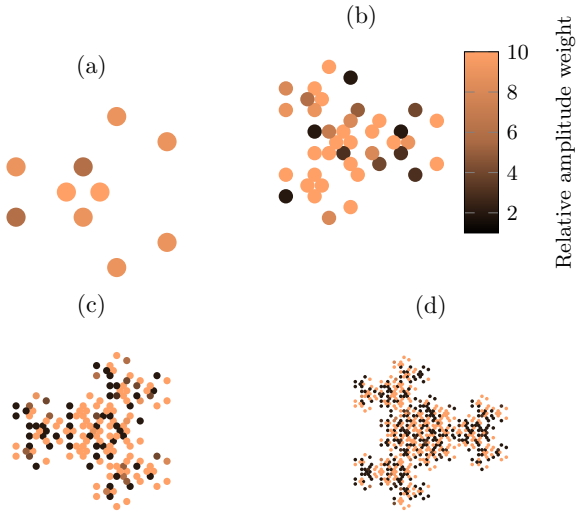


Figure 10. Optimized array layout and relative amplitude weights for Design A: (**a**) growth stage 2 and 10 active elements, (**b**) growth stage 3 and 40 active elements, (**c**) growth stage 4 and 160 active elements, (**d**) growth stage 5 and 640 active elements.

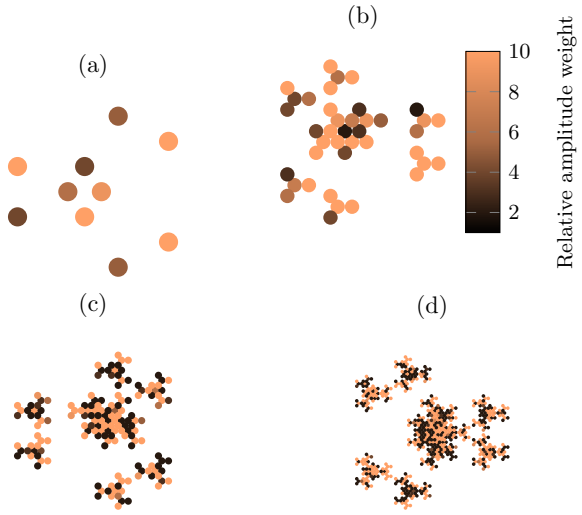


Figure 11. Optimized array layout and relative amplitude weights for Design B: (**a**) growth stage 2 and 10 active elements, (**b**) growth stage 3 and 40 active elements, (**c**) growth stage 4 and 160 active elements, (**d**) growth stage 5 and 640 active elements.

Table 4 presents the obtained best relative amplitude configuration for each Eisenstein fractal stage to recreate Design A and Design B, with turned-off elements having values of zero.

Table 4. Optimized amplitude excitation weights for each fractal stage in Design A and Design B. Zero values denote inactive elements.

Stage	Design A	Design B
2	[10,0,9,6,0,9,9,0,0,10,6,9,0,9,0,9]	[9,0,10,4,0,10,5,0,0,6,4,10,0,10,0,5]
3	[10,0,3,10,0,4,10,0,0,10,10,2,0,10,0,5, 10,0,10,10,0,10,8,0,0,10,2,10,0,10,0,10, 10,0,9,10,0,8,7,0,0,6,9,8,0,2,0,10, 9,0,3,2,0,10,3,0,0,10,8,10,0,10,0,4]	[10,10,4,2,0,0,0,0,10,10,10,4,9,5,3,3, 0,0,0,0,10,10,4,10,7,10,6,3,0,0,0,0, 0,0,0,0,9,7,10,10,4,6,4,10,6,10,10,10, 0,0,0,0,10,10,10,10,0,0,0,0,9,10,6,2]
4	[10,0,10,2,0,2,2,0,0,9,10,10,0,10,0,2, 10,0,10,10,0,10,2,0,0,10,10,2,0,10,0,2, 10,0,10,10,0,10,10,0,0,10,2,2,0,10,0,10, 10,0,2,10,0,10,10,0,0,2,10,10,0,2,0,10, 2,0,2,2,0,10,2,0,0,10,2,2,0,10,0,5, 10,0,4,2,0,10,2,0,0,5,10,10,0,10,0,10, 10,0,10,5,0,10,2,0,0,2,2,2,0,4,0,9, 10,0,2,2,0,10,10,0,0,10,2,10,0,10,0,10, 10,0,10,10,0,9,2,0,0,10,2,2,0,10,0,10, 10,0,2,10,0,9,2,0,0,10,4,10,0,10,0,3, 10,0,2,10,0,4,2,0,0,2,6,2,0,6,0,10, 2,0,4,10,0,10,10,0,0,10,2,4,0,10,0,2, 10,0,6,5,0,10,2,0,0,10,10,10,0,10,0,10, 10,0,2,2,0,10,10,0,0,7,10,10,0,5,0,2, 10,0,2,10,0,10,10,0,0,10,2,2,0,10,0,10, 10,0,2,10,0,10,10,0,0,10,10,2,0,8,0,4]	[10,2,2,2,10,10,2,2,2,10,10,10,2,10,10,2, 0,0,0,0,0,0,0,0,0,0,0,0,0,0,0,0, 10,10,3,2,10,10,3,2,10,10,9,10,2,2,2,10, 2,10,10,2,10,10,2,2,10,10,2,10,10,5,2,2, 0,0,0,0,0,0,0,0,0,0,0,0,2,4,10,10, 10,10,2,2,2,3,2,10,10,10,10,10,10,2,2,2, 10,5,10,2,10,2,3,10,3,6,3,9,0,0,0,0, 0,0,0,0,0,0,0,0,0,0,0,0,0,0,0,0, 0,0,0,0,0,0,0,0,5,10,10,10,2,2,10,10, 10,2,2,10,10,2,2,10,10,2,3,2,10,2,2,2, 2,2,3,10,10,10,2,10,6,2,2,10,10,3,6,10, 3,10,10,2,2,10,10,2,0,0,0,0,0,0,0,0, 0,0,0,0,0,0,0,0,0,0,10,10,10,10,2,2, 10,6,10,2,2,2,10,10,2,10,0,0,0,0,0,0, 0,0,0,0,0,0,0,0,0,0,10,2,2,10,3,10,10, 10,2,10,9,2,2,2,2,2]

The array factor response at each stage is illustrated in Figure 12 at the lower frequency f_l. Design A demonstrates superior performance in terms of capacity, exhibiting a more uniformly distributed radiation pattern. Proposed designs present a narrowing of the main beam in the early stages and a notable suppression of secondary lobes while significantly reducing the number of active elements. These benefits are achieved while preserving the wideband characteristics and maintaining a streamlined geometry and radiation response.

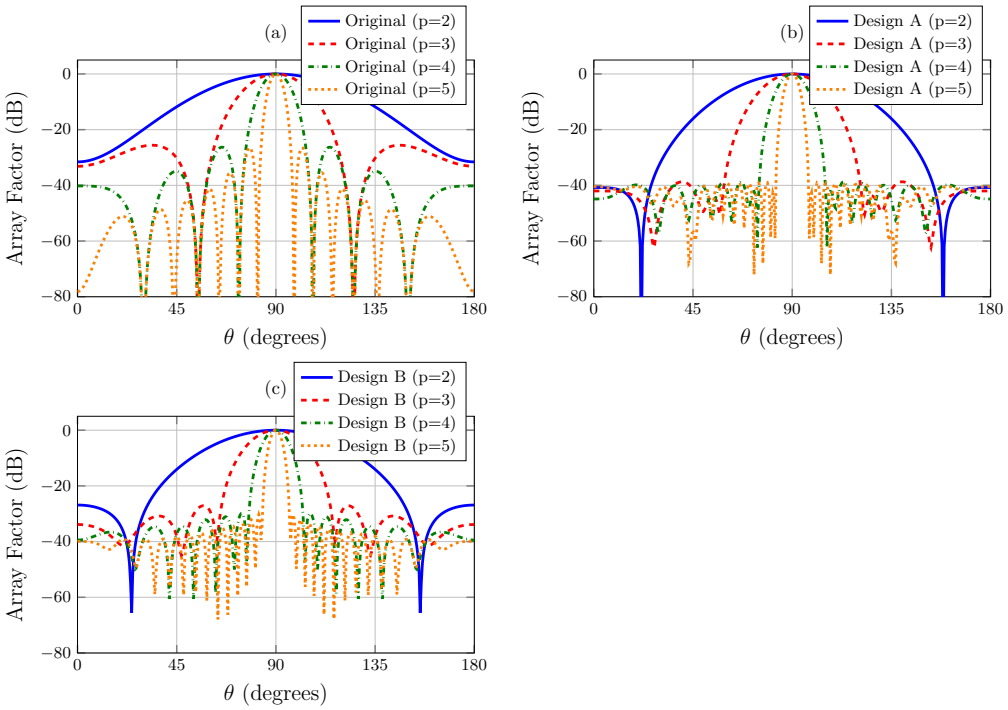


Figure 12. Array factor patterns comparing different stages for (**a**) Original design, (**b**) Design A, and (**c**) Design B at initial operation frequency f_1.

A comparison between the original Eisenstein array comprising the complete set of antenna elements and the optimized designs with reduced element counts and adjusted relative amplitude values reveals improved performance in SLL suppression across multiple operational frequencies. The optimized configurations either reduce or maintain a comparable HPBW relative to the original full-element structure. These performance enhancements are summarized in Table 5, which provides detailed quantitative data supporting the effectiveness of the proposed design strategies.

Table 5. Comparative performance of proposed wideband optimized designs with original base Eisenstein fractile with complete structure and uniform amplitudes.

Stage	d/λ	Original			Design A			Design B	
		Elements	SLL (dB)	HPBW (°)	Elements	SLL (dB)	HPBW (°)	SLL (dB)	HPBW (°)
2	0.5	ON	$-\infty$	63.33	ON	−40.77	55.82	−26.87	59.83
	1	16	−22.60	30.29	10	−15.69	26.78	−23.24	28.79
	1.5	OFF	−22.60	19.77	OFF	−15.69	17.27	−23.24	18.77
	2	0	−8.64	14.77	6	−13.35	13.26	−9.94	14.26
3	0.5	ON	−25.59	29.79	ON	−38.72	28.79	−27.11	27.28
	1	64	−25.59	14.77	40	−21.29	14.26	−27.12	13.26
	1.5	OFF	−25.59	9.76	OFF	−19.25	9.26	−27.11	8.76
	2	0	−25.58	7.26	24	−19.25	6.75	−27.14	6.75
4	0.5	ON	−26.29	14.26	ON	−38.74	14.26	−29.86	13.26
	1	256	−26.28	7.26	160	−34.96	7.26	−29.85	6.25
	1.5	OFF	−26.28	4.75	OFF	−34.54	4.75	−29.83	4.25
	2	0	−26.27	3.25	96	−34.55	3.25	−29.85	3.25
5	0.5	ON	−26.46	7.26	ON	−39.01	7.26	−30.30	6.25
	1	1024	−26.44	3.25	640	−35.42	3.25	−30.26	3.25
	1.5	OFF	−26.45	2.25	OFF	−34.85	2.25	−30.39	2.25
	2	0	−26.49	1.75	384	−34.82	1.75	−30.34	1.25

4. Discussion

The multi-objective implementation presents designs that exhibit efficient SLL suppression and stable wideband performance, even with a reduced number of active elements. These findings underscore the advantages of integrating Eisenstein fractal symmetry with evolutionary optimization techniques, facilitating the development of compact, efficient, and high-performance antenna array designs.

The proposed Design A, based on the thinned Eisenstein fractal structure, exhibits superior SLL reduction across all evaluated frequency bands when compared to various recent studies on wideband antenna array optimization. Table 6 presents a detailed performance comparison, emphasizing the advantages of Design A over other wideband-optimized array designs that employ different geometries and optimization methodologies. Notably, Design A achieves its strongest performance at the foundational operating frequency (0.5λ), where it not only surpasses most existing designs in terms of SLL reduction but also does so using fewer active elements, underscoring its efficiency and effectiveness.

Evaluated normalized performance metrics such as SLL and HPBW were the focus as they are directly affected by the array synthesis method. The normalized gain is inherently linked to these metrics, which serves as an indicator of directional performance in an idealized context. In contrast, realized gain accounts for practical considerations such as element efficiency, mutual coupling, impedance matching, and feed network losses, which are not addressed in the present analysis.

Table 6. Comparison of SLL performance at different normalized frequencies between the proposed designs and state-of-the-art wideband antenna arrays based on various geometries and optimization methods.

Ref.	Array Geometry	Elements	SLL (dB)		
			0.5λ	1.0λ	1.5λ
[13]	Perturbed Peano–Gosper curve	50	−8.11	−7.71	−7.71
		344	−10.12	−9.71	−9.71
[33]	Symmetric sparse circular arrays	600	−20.22	−18.99	−18.99
[34]	Fractal pentagonal	13	−17.64	−17.64	−17.64
		49	−23.12	−23.12	−23.12
		162	−28.43	−28.43	−28.43
[17]	Non-uniform concentric rings	90	−24.95	−10.21	−10.21
		168	−26.59	−12.24	−12.24
[18]	Fermat spiral	64	−8.48	−8.26	−8.26
		256	−14.01	−13.26	−13.26
[22]	Eisenstein fractile	16	−22.61	−22.61	−22.61
		64	−25.59	−25.60	−25.59
[22]	Thinned Eisenstein Fractile	10	−34.65	−13.98	−13.98
		40	−32.04	−13.98	−13.98
This work	Improved thinned Eisenstein fractile	10	−40.77	−15.69	−15.69
		40	−38.72	−21.29	−19.25
		160	−38.74	−34.96	−34.54

The proposed Eisenstein fractal-based array designs exhibit unidirectional radiation characteristics with narrow main beams, making them particularly suitable for applications requiring spatial interference suppression and precise angular targeting, such as radar systems, directional IoT links, or satellite [35,36]. As the fractal stage increases, the SLL improves, while the beam becomes narrower, which may impact performance in certain

wide-coverage scenarios. Potential solutions to address this trade-off may include adjusting the mask function to desired beam width, incorporating adaptive beamforming techniques, or using multiple array configurations to achieve desired coverage.

The optimization framework can be generalized to other aperiodic array geometries and allows for straightforward adaptation to alternative algorithms, depending on the problem complexity or convergence requirements. This flexibility makes the methodology broadly applicable to diverse array synthesis scenarios. The computational demands remain manageable for even large-scale arrays, due to the decoupled optimization stages and the use of lightweight evaluation metrics. Improvements in runtime can be achieved by incorporating Machine Learning and GPU acceleration techniques, strengthening the suitability for real-time applications or large-dimensional antenna design tasks.

5. Conclusions

This study presents a synthesis framework for thinned wideband antenna arrays by integrating fractal Eisenstein geometry with advanced multi-objective evolutionary optimization techniques. Exploiting the inherent self-similarity properties of the Eisenstein fractal structure, combined with algorithms such as MO-BDE and MO-PSO, the proposed method successfully reduced the number of active elements by up to 37.5%, without compromising performance across the wideband frequency range.

Two distinct design cases were evaluated. Design A, optimized for a primary operational frequency, achieved an SLL reduction of approximately 12 dB compared to the original structure, demonstrating its suitability for high precision demanding scenarios. In contrast, Design B maintained a consistent SLL reduction of up to -3 dB across the bandwidth, offering well-balanced performance for multiband and frequency-agile systems.

The findings validate the effectiveness of combining fractal geometries with evolutionary algorithms to achieve efficient array thinning while preserving beamforming and spectral integrity. This work advances the theoretical foundations of fractal-based antenna synthesis and offers practical pathways for implementing energy-efficient, high-performance arrays in next-generation technologies. Future research should explore the integration of these optimized arrays into real-world devices and communication platforms such as MIMO radar systems, which benefit from self-similar geometries, and IoT devices that demand compact, wideband, and interference-resilient antenna solutions.

Author Contributions: Conceptualization, L.A.G.; Methodology, L.A.G. and M.A.P.; Software, L.E.C.; Validation, M.A.P., A.R. and M.A.Z.; Formal analysis, L.E.C., L.A.G. and M.A.P.; Investigation, L.E.C. and L.A.G.; Resources, L.A.G. and A.R.; Data curation, L.E.C. and L.A.G.; Writing—original draft, L.E.C.; Writing—review & editing, L.A.G., M.A.P. and A.R.; Visualization, L.E.C. and L.A.G.; Supervision, L.A.G. and M.A.P.; Project administration, L.A.G.; Funding acquisition, L.A.G. All authors have read and agreed to the published version of the manuscript.

Funding: This research was funded by Consejo Nacional de Ciencia y Tecnología (CONACYT), through scholarship grant number 833095.

Institutional Review Board Statement: Not applicable.

Informed Consent Statement: Not applicable.

Data Availability Statement: The original contributions presented in this study are included in the article. Further inquiries can be directed to the corresponding author.

Conflicts of Interest: The authors declare no conflicts of interest.

References

1. Wang, C.-X.; Feng, R.; Sun, H.; Liu, J.; Xie, Y.; Gao, X.; Liu, L.; Li, Y.; Wang, M.; You, X.; et al. On the Road to 6G: Visions, Requirements, Key Technologies and Testbeds. *arXiv* **2023**, arXiv:2302.14536. [CrossRef]
2. Figueiredo, F.A.P. An Overview of Massive MIMO for 5G and 6G. *IEEE Lat. Am. Trans.* **2022**, *20*, 931–940. [CrossRef]
3. Reddy, M.H.; Sheela, D. MIMO antenna design and optimization with enhanced bandwidth for wireless applications. *J. Telecommun. Inf. Technol.* **2020**, *4*, 22–26. [CrossRef]
4. Karmakar, A. Fractal antennas and arrays: A review and recent developments. *Int. J. Microw. Wirel. Technol.* **2021**, *13*, 173–197. [CrossRef]
5. Chand Ravi, K.; Kumar, J.; Elwi, T.A.; Mahdi Ali, M. Compact MIMO antenna for 5G Applications. In Proceedings of the 2022 IEEE ANDESCON, Quito, Ecuador, 13–15 October 2022; IEEE: Piscataway, NJ, USA, 2022; pp. 1–4. [CrossRef]
6. Palanisamy, S.; Thangaraju, B.; Khalaf, O.I.; Alotaibi, Y.; Alghamdi, S.; Alassery, F. A novel approach of design and analysis of a hexagonal fractal antenna array (HFAA) for next-generation wireless communication. *Energies* **2021**, *14*, 6204. [CrossRef]
7. Hohlfeld, R.G.; Cohen, N. Self-similarity and the geometric requirements for frequency independence in antennas. *Fractals* **1999**, *7*, 79–84. [CrossRef]
8. Anguera, J.; Puente, C.; Borja, C.; Soler, J. Fractal antennas: An historical perspective. *Fractal Fract.* **2020**, *4*, 3. [CrossRef]
9. Spence, T.G.; Werner, D.H. Design of broadband planar arrays based on the optimization of aperiodic tilings. *IEEE Trans. Antennas Propag.* **2008**, *56*, 76–86. [CrossRef]
10. Hussein, R.T.; Jibrael, F.J. Comparison of the radiation pattern of fractal and conventional linear array antenna. *Prog. Electromagn. Res. Lett.* **2008**, *4*, 183–190. [CrossRef]
11. Werner, D.H.; Kuhirun, W.; Werner, P.L. A new design methodology for modular broadband arrays based on fractal tilings. In Proceedings of the 2003 IEEE Topical Conference on Wireless Communication Technology, Honolulu, HI, USA, 15 October 2003; pp. 267–268. [CrossRef]
12. Werner, D.H.; Kuhirun, W.; Werner, P.L. Fractile arrays: A new class of tiled arrays with fractal boundaries. *IEEE Trans. Antennas Propag.* **2004**, *52*, 2008–2018. [CrossRef]
13. Spence, T.G.; Werner, D.H.; Carvajal, J.N. Modular broadband phased-arrays based on a nonuniform distribution of elements along the peano-gosper space-filling curve. *IEEE Trans. Antennas Propag.* **2010**, *58*, 600–604. [CrossRef]
14. Gregory, M.D.; Namin, F.A.; Werner, D.H. Exploiting rotational symmetry for the design of ultra-wideband planar phased array layouts. *IEEE Trans. Antennas Propag.* **2013**, *61*, 176–184. [CrossRef]
15. Ponnapalli, V.A.S.; Jayasree, P.V.Y. Heptagonal fractal antenna array for wireless communications. In *Advances in Signal Processing and Communication*; Reddy, P.S., Thangavel, M., Prabhakar, S., Eds.; Springer: New Delhi, India, 2016; pp. 387–394. [CrossRef]
16. El-Khamy, S.E.; Eltrass, A.S.; El-Sayed, H.F. Generator optimization for thinned fractal hexagonal and pentagonal antenna arrays using Ant Colony algorithm. In Proceedings of the 2017 34th National Radio Science Conference (NRSC), Alexandria, Egypt, 13–16 March 2017; pp. 71–78. [CrossRef]
17. Panduro, M.A.; Reyna, A.; Covarrubias, D.H. Non-Uniform Concentric Rings Design for Ultra-Wideband Arrays. *Sensors* **2019**, *19*, 2262. [CrossRef] [PubMed]
18. Liu, S.; Chen, L.; Liu, Y. Design of Parameter-Optimized Spiral Arrays with Ultra-Wideband Grating Lobe Suppression. *Electronics* **2023**, *12*, 1664. [CrossRef]
19. Dahl, C.; Vogt, M.; Rolfes, I. A MIMO Radar System based on Fractal Antenna Arrays for Level Measurement Applications. *Adv. Radio Sci.* **2021**, *19*, 23–29. [CrossRef]
20. Dong, Y.; Cai, X.; Geyi, W. A Weighted Method for Multi-Beam Synthesis with Controllable Gain and Sidelobe Suppression. *IEEE Trans. Antennas Propag.* **2025** . [CrossRef]
21. Beccaria, M.; Massaccesi, A.; Pirinoli, P.; Manh, L.H. Multibeam Transmitarrays for 5G Antenna Systems. In Proceedings of the 2018 IEEE International Conference on Communications and Electronics (ICCE), Hue, Vietnam, 18–20 July 2018; pp. 217–221.
22. El-Khamy, S.E.; El-Sayed, H.F.; Eltrass, A.S. Synthesis of Wideband Thinned Eisenstein Fractile Antenna Arrays with Adaptive Beamforming Capability and Reduced Side-Lobes. *IEEE Access* **2022**, *10*, 122486–122500. [CrossRef]
23. Helmberg, G. On the Eisenstein Packing of the Complex Plane. *Math. Intell.* **2015**, *37*, 27–33. [CrossRef]
24. Balanis, C.A. *Antenna Theory: Analysis and Design*, 4th ed.; Wiley: Hoboken, NJ, USA, 2016.
25. Stutzman, W.L.; Thiele, G.A. *Antenna Theory and Design*, 3rd ed.; Wiley: Hoboken, NJ, USA, 2013.
26. Eberhart, R.C.; Shi, Y. Particle Swarm Optimization: Developments, Applications and Resources. In Proceedings of the 2001 Congress on Evolutionary Computation (CEC2001), Seoul, Republic of Korea, 27–30 May 2001; pp. 81–86. [CrossRef]
27. Pampará, G.; Engelbrecht, A.P.; Franken, N. Binary Differential Evolution. In Proceedings of the 2006 IEEE Congress on Evolutionary Computation, Vancouver, BC, Canada, 16–21 July 2006; pp. 1873–1879. [CrossRef]
28. Schlosser, E.R.; Tolfo, S.M.; Heckler, M.V.T. Particle Swarm Optimization for antenna arrays synthesis. In Proceedings of the 2015 SBMO/IEEE MTT-S International Microwave and Optoelectronics Conference (IMOC), Porto de Galinhas, Brazil, 3–6 November 2015; pp. 1–6. [CrossRef]

29. Alnahwi, F.M.; Al-Yasir, Y.I.A.; Sattar, D.; Ali, R.S.; See, C.H.; Abd-Alhameed, R.A. A New Optimization Algorithm Based on the Fungi Kingdom Expansion Behavior for Antenna Applications. *Electronics* **2021**, *10*, 2057. [CrossRef]
30. Petko, J.S.; Werner, D.H. The Pareto optimization of ultrawideband polyfractal arrays. *IEEE Trans. Antennas Propag.* **2008**, *56*, 97–107. [CrossRef]
31. Deligkaris, K.V.; Zaharis, Z.D.; Kampitaki, D.G.; Goudos, S.K.; Rekanos, I.T.; Spasos, M.N. Thinned Planar Array Design Using Boolean PSO with Velocity Mutation. *IEEE Trans. Magn.* **2009**, *45*, 1490–1493. [CrossRef]
32. Mondal, A.K.; Saxena, P. Thinning of Concentric Circular Antenna Array Using Binary Salp Swarm Algorithm. In Proceedings of the 2019 IEEE Conference on Information and Communication Technology (CICT), Allahabad, India, 6–8 December 2019; pp. 1–4. [CrossRef]
33. Wang, R.Q.; Jiao, Y.C. Synthesis of Wideband Rotationally Symmetric Sparse Circular Arrays with Multiple Constraints. *IEEE Antennas Wirel. Propag. Lett.* **2019**, *18*, 821–825. [CrossRef]
34. El-Khamy, S.E.; Eltrass, A.S.; El-Sayed, H.F. Design of thinned fractal antenna arrays for adaptive beam forming and sidelobe reduction. *IET Microwaves Antennas Propag.* **2018**, *12*, 435–441. [CrossRef]
35. Kundu, K.; Rai, A.; Singh, R.P. Role of IoT and Antenna Array in Smart Communication and 5G. In *Paradigms of Smart and Intelligent Communication, 5G and Beyond*; Rai, A., Kumar Singh, D., Sehgal, A., Cengiz, K., Eds.; Transactions on Computer Systems and Networks; Springer: Singapore, 2023; pp. 41–58. [CrossRef]
36. Kedar, A. Phased Array Antenna for Radar Application. In *Handbook of Metrology and Applications*; Aswal, D.K., Yadav, S., Takatsuji, T., Rachakonda, P., Kumar, H., Eds.; Springer: Singapore, 2023; pp. 811–828. [CrossRef]

Disclaimer/Publisher's Note: The statements, opinions and data contained in all publications are solely those of the individual author(s) and contributor(s) and not of MDPI and/or the editor(s). MDPI and/or the editor(s) disclaim responsibility for any injury to people or property resulting from any ideas, methods, instructions or products referred to in the content.